Supplementary information

# Linear, symmetric, self-selecting 14-bit molecular memristors

Deepak Sharma[1], Santi Prasad Rath[1], Bidyabhusan Kundu[1], Anil Korkmaz[2], Damien Thompson[3], Navakanta Bhat[1], Sreebrata Goswami[1], R Stanley Williams[2] and Sreetosh Goswami[1]

1. Centre for Nanoscience and Engineering, Indian Institute of Science, Bangalore 560012, India
2. Department of Electrical and Computer Engineering, Texas A&M University, College Station, TX 3127, USA
3. Department of Physics, University of Limerick, Limerick, V94 T9PX, Ireland

## Section S1: Materials, and film characterization

### Materials preparation:

$[Ru^{II}L_2](BF_4)_2$ (L = 2,6-bis(phenylazo)pyridine) was synthesized using methods described in[1,2].

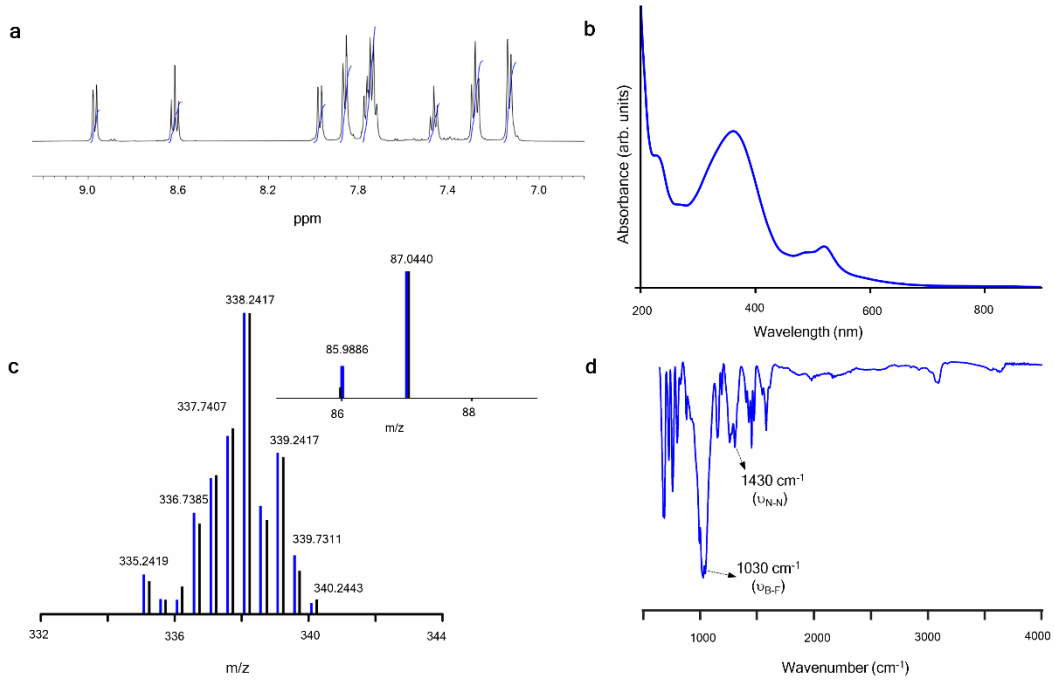


**Figure S1: Chemical Characterization of the ruthenium complex:**

(a) Segmented $^1H$ NMR spectra of $[RuL_2](BF_4)_2$ in $CD_3CN$ solvent using a 500 MHz spectrometer.
(b) The UV-Vis spectrum of the complex. The peak positions are consistent with the prior reports[2].
(c) Segmented electrospray ionisation mass spectrometry (ESI-MS) spectrum where the inset shows the mass fragments in the negative mode. The experimental and simulated spectra of the individual fragments coloured black and blue, respectively, showing close match between measured and expected values.
(d) Attenuated total reflectance-Fourier transform infrared (ATR-FTIR) spectrum where the N-N azo stretching frequencies in the molecule and the B-F stretching frequencies in the $BF_4$ counterion (Fig.1a in main text) are marked.

These characterizations confirm the purity of our material.

**Crossbar fabrication:**

The crossbar and the molecular films were made using optimised protocols described in our earlier studies[2–4].

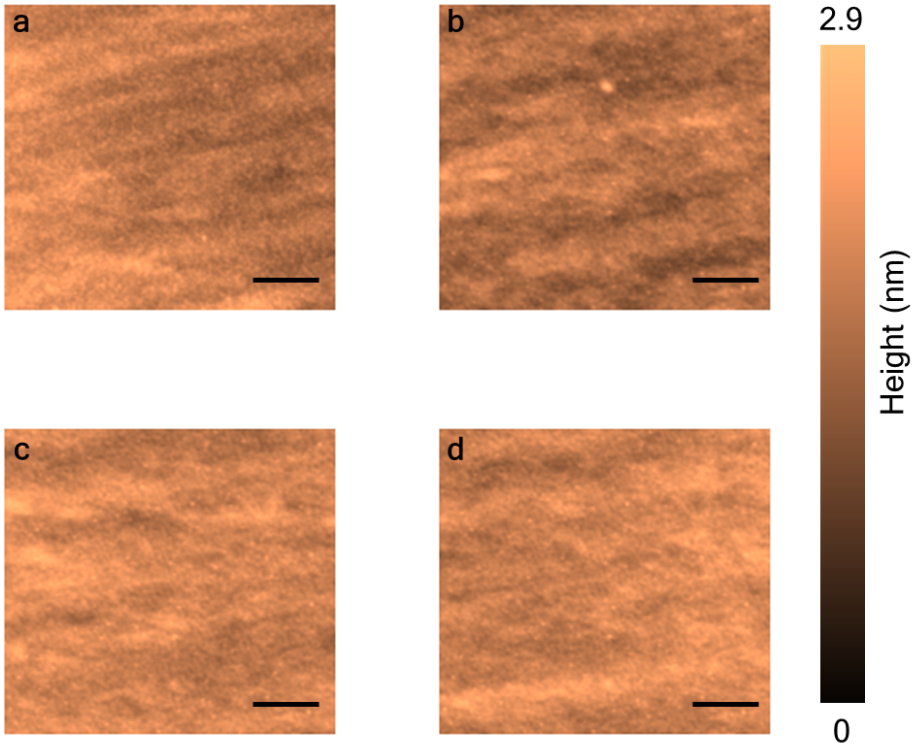


**Figure S2: Atomic force microscopy (AFM) images of our molecular film:** (a-d) Four different 25µm × 25µm areas on the film were randomly chosen and their AFM images show consistent root mean square (RMS) roughness of (a) 0.88 nm, (b) 0.94 nm, (c) 0.92nm, and (d) 0.97 nm. The scale bar is 5µm.

## Section S2: Electrical measurement set up

**A mixed signal programmable circuit board –**

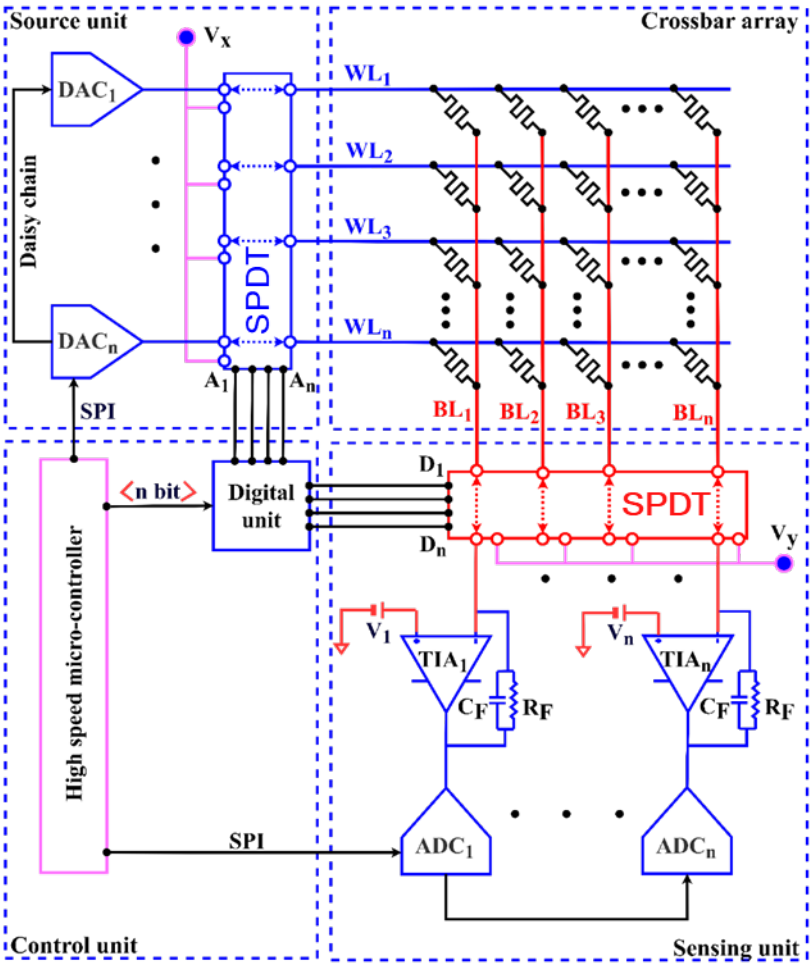


**Figure S3: Electrical measurement circuit:** The layout of the electrical circuit used for characterizing our analog crossbar.

A mixed-signal printed circuit board (PCB) was developed for writing and reading the crossbar with >16-bit accuracy over the conductance range of 200 nS to 5.9 mS. The PCB comprises the following units (Fig. S3):

**Control unit:** The control unit is made of a microcontroller and a digital unit as shown in Fig. S3.

1. **Digital unit –** Based on a pulse generator circuit, made with logic gates, flip-flops and a microcontroller. The microcontroller communicates with other components via serial peripheral interface (SPI) and Inter-Integrated Circuit ($I^2C$) protocols. This unit can generate simultaneous pulses to feed up to 64 channels with a resolution of <2 ns.

2. **Microcontroller –** We used an Arduino board which is based on a 32-bit ARM core microcontroller that runs on an 84 MHz clock. All components were controlled using standard communication protocols, namely, SPI and $I^2C$.

**Source unit –** Source unit consists of multichannel digital to analog converters (DAC) with at least 16 bits of specified resolution.

**Switches –** Each row and column in the memristor array was independently controlled using analog Single Pole Double Throw (SPDT) switches with leakage <3pA. The selection lines of these multichannel parallel switches were synchronised with the digital unit and firmware.

**Crossbar array –** The crossbar was die-attached to a customized breakout board and connected via 25 μm gold wire bonding. The breakout board, soldered with gold berg connectors, was then plugged into the main data acquisition board.

**Sensing unit –** This consists of precision transimpedance amplifiers (TIAs). The TIA outputs are connected to analog to digital convertors with 24 bits of specified resolution.

For writing a chosen cross point, the corresponding word line was connected to the DAC output (programmed at 3.9 V) and the bit line was tethered to the virtual ground of the TIA (set at 3 V) using SPDT switches. All other word and bit lines were maintained at a half-select voltage of 450 mV (in Fig. S3, $V_x = V_y = 450mV$). As shown in Fig. 2d, any applied voltage lower than 830 mV does not cause a change in the cross-point conductance. The half select protocol[3-5] ensured that the cross points other than the selected one were not disturbed.

A custom C++ based firmware was developed to ensure the operational accuracy of the PCB and to enable communication with an external PC for further data analysis. The board was calibrated against precision measurement instruments including UFHLI Lock-in Amplifier (Zurich instruments) and SHFSG Signal generator (Zurich Instruments).

## Section S3: Electrical characterization of individual cross points

### Measurement of row and column wire conductance values:

To accurately determine the conductance of individual cross points in a crossbar, it is necessary to know the wire conductance/resistance. The wire resistance along the rows and columns were measured using a 4-probe resistance measurement technique (see Fig. S4). Resistance values were measured for the entire lengths of the rows and columns ($R_R$, $R_c$ for lengths $L_R$ and $L_C$), and then scaled to the separation 'd' ($d_R$, $d_C$) to determine the resistance between the cross points:

Inter-cross-point row resistance $\rho = R_R \times \frac{d_R}{L_R}$ (S1)

Inter-cross-point column resistance $\chi = R_C \times \frac{d_C}{L_C}$ (S2)

In our crossbar, $\rho$ = 0.46 Ω and $\chi$ = 0.39 Ω

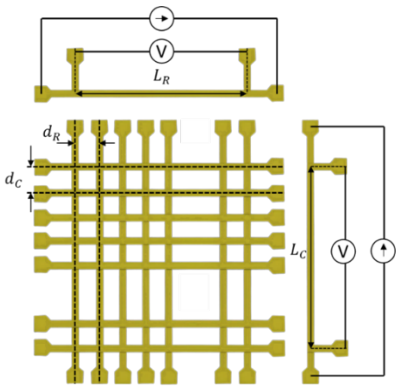


**Figure S4: Characterization of crossbar wire resistance:** Four probe measurements to characterize the wire resistance of the rows and columns of the crossbar.

### Accurate writing of the crossbar elements:

Each element in the crossbar was written individually. Using the single pole double throw (SPDT) switches (Fig. S3) along the rows and columns, the element to be written was chosen. For the duration when these SPDT switches are ON (controlled by the digital unit, see Fig. S3), the top electrode of the element would be connected to the DAC output and the bottom electrode would be grounded through the non-inverting terminal for the transimpedance amplifier (TIA) (see Fig. S3). The memristor current is fed to the inverting TIA terminal which gets converted to the output voltage.

The voltage across the targeted memristor junction is reduced from the intended value due to the resistances in both the row and column wires. To ensure that the desired voltage appears across the chosen memristor, the applied voltage was scaled considering the series wire resistances. For writing the $M_{p,q}$ element (i.e., the element at the junction of $p^{th}$ row and $q^{th}$ column), the modified applied voltage is:

$$V'_{Wp} = V_{Gq} + V_{Wp} \times \vartheta, \quad \text{(S3)}$$

where $\vartheta$ is the scaling factor given by $\vartheta = \left(1 + \frac{q\rho+(N-p+1)\chi}{R_{p,q}}\right)$.

Here, $V_{Gq}$= voltage applied at the TIA non-inverting terminal, $V_{Wp}$ = the writing voltage required to appear across the memristor, $N$ = crossbar size (i.e., the total number of rows and columns, for a square crossbar), $V'_{Wp}$= modified writing voltage taking the row and column resistances into consideration. $\rho$ and $\chi$ are the inter-cross-point resistances. This formulation is consistent with previous reports[6,7].

We used the microcontroller to compute the scaling factor for each applied voltage. This process needs to be done only once during writing and can subsequently be used for as many reading cycles as required. We applied 450mV in all the unselected rows and columns. This resulted in an excellent write accuracy with a root mean square error RMSE = $\sqrt{\frac{\sum_{i=1}^{n}(G_n - G_{n,target})^2}{N_L}}, \forall\, n \in [1,16520], N_L = 16520$ (where $G_n$ was the written conductance for the $n^{\text{th}}$ level and $G_{n,target}$ was the target value) of ~40nS, as shown in Fig. S5.

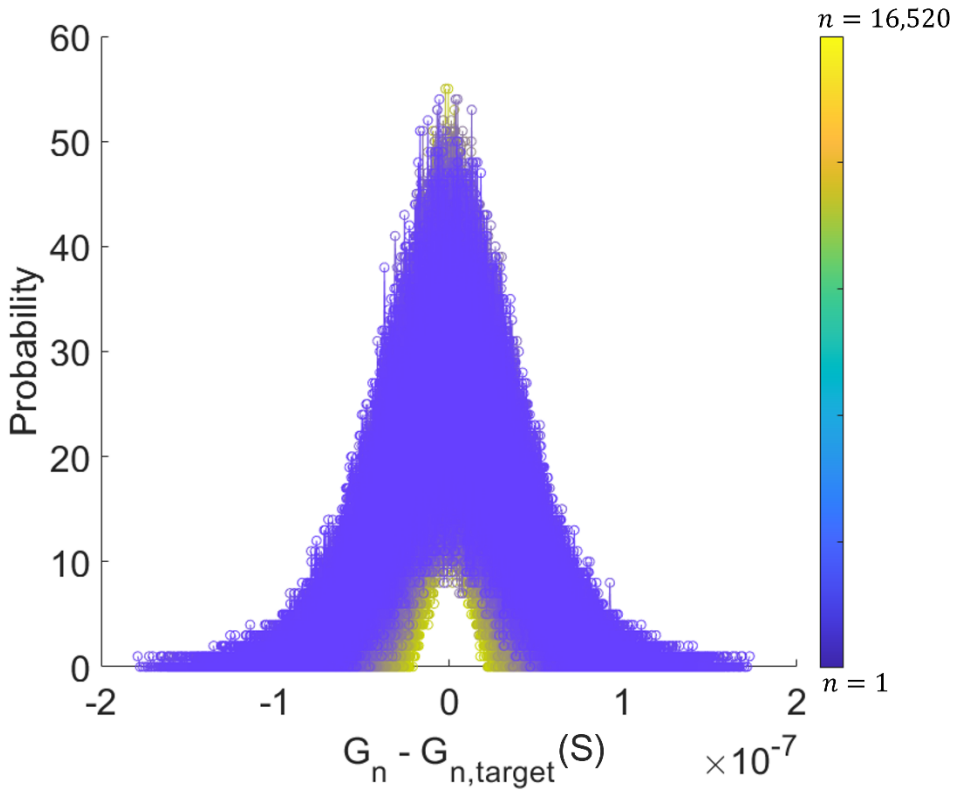


**Figure S5: Reading accuracy:** The distribution of 16,520 the states (written using eqn. S1-S3) *w.r.t.* the target values. Each distribution was based on 2000 independent measurement points.

**Reading the accurate conductance of the individual crossbar elements:**

For reading a particular element in a crossbar, $M_{p,q}$, the row and the column (*i.e.*, $p^{th}$ and $q^{th}$) needs to be selected by the SPDT switches shown in Fig. S3. The measured current will be affected by the wire resistances along the rows and the columns.

Taking those into consideration $R_{p,q}$ can be determined from the measured current using the following equation,

$$R_{p,q} = \frac{(V_{Rp} - V_{Gq})}{I_q} - (N - p + 1)\chi + q\rho \quad , \qquad \text{(S4)}$$

where $V_{Rp}$ = Applied reading voltage to the $p^{th}$ row, $V_{Gq}$= voltage applied at the TIA non-inverting terminal, $I_q$ = Current measured at the $q^{th}$ column, $N$= crossbar size (i.e., the total number of rows/ columns), and $\rho$ and $\chi$ are defined in eqn. (S1) and (S2), respectively. This computation was performed at the microcontroller to accurately determine the potentiation-depression characteristics of individual cross points. For reading we used both a floating scheme (where the unselected rows and columns were kept floating) or a half-select approach (with half-select voltage of 250 mV), identical to the one described during the writing process both yielding similar outputs[3-5].

For more realistic application scenarios, parallel reading would be required (such as in Fourier transformation). For that, we used the formulation presented in section S5.

**Estimated read accuracy:**

After compensating the effect of the wire resistances described above, the conductance values in a crossbar were compared with a single isolated device measurement. As shown in Fig. S6, the weight update characteristics from a single device are the same as those obtained from different locations of the crossbar, confirming the reliability of our measurements and wire resistance compensation scheme.

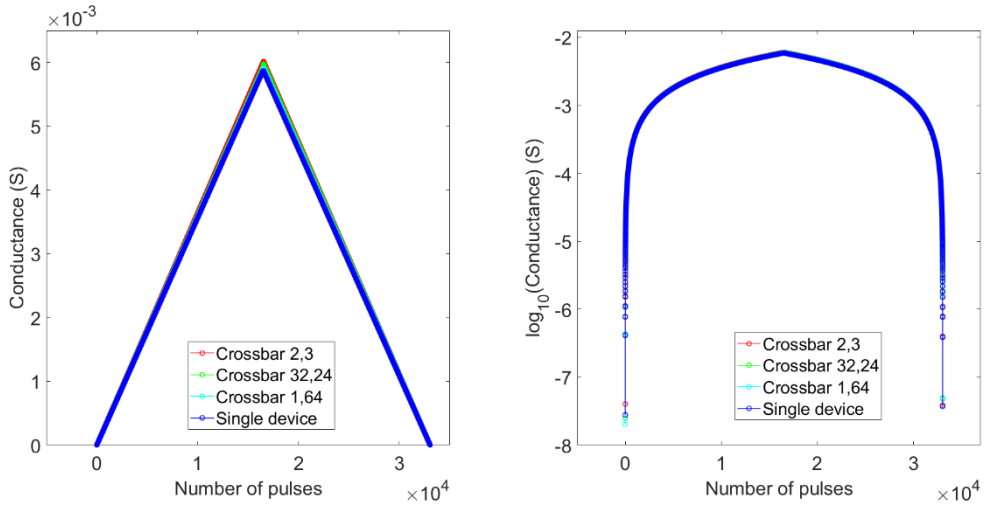


**Figure S6: Reading accuracy:** Comparison between the weight update characteristics obtained from a single device to those measured at different locations in a crossbar after compensating the effect of wire resistance.

Also, we note that the linearity and symmetry in the weight update characteristics is valid for various conductance ranges. The history of potentiation is retained and determines the depression characteristic.

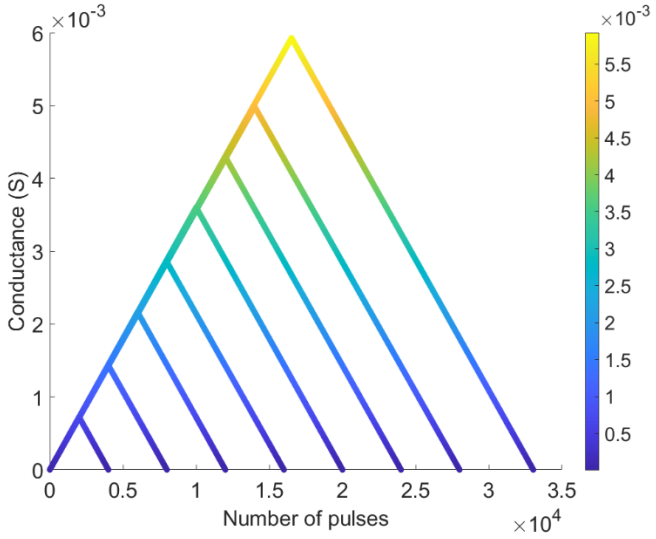


**Figure S7: Weight update for different ranges:** The weight update characteristics for different conductance ranges.

**Nonlinearity beyond 16520 cycles:**

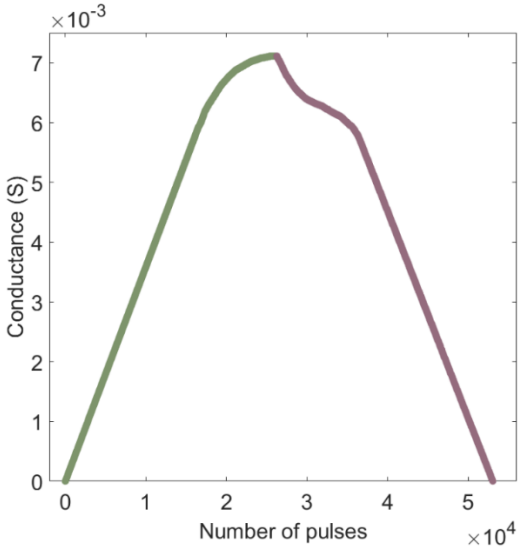


**Figure S8: Deviation from zeroth order process at higher conductance:** When we keep pulsing the system beyond 16,520 pulses, the weight update process loses linearity and exhibits saturation. This is caused by the eventual exhaustion of the 31 state and predominance of 22 inside the molecular film.

**Reliability of the cross points and the measurement technique:**

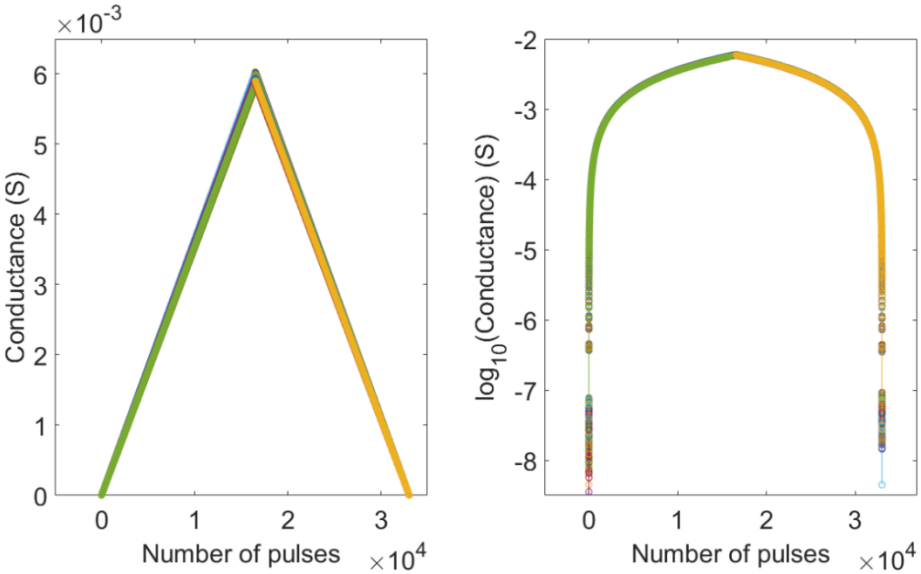


**Figure S9: Characteristics from 900 cross points:** 9,000 weight update characteristics from 900 cross points (each measured 10 times) are overlaid exhibiting performance consistency, uniformity, and the reliability of our measurement protocols. Different colours are used for potentiation and depression. It also shows the reliability of our measurement protocols. The wire resistance was compensated using equation S4.

**Unidirectional read-out:**

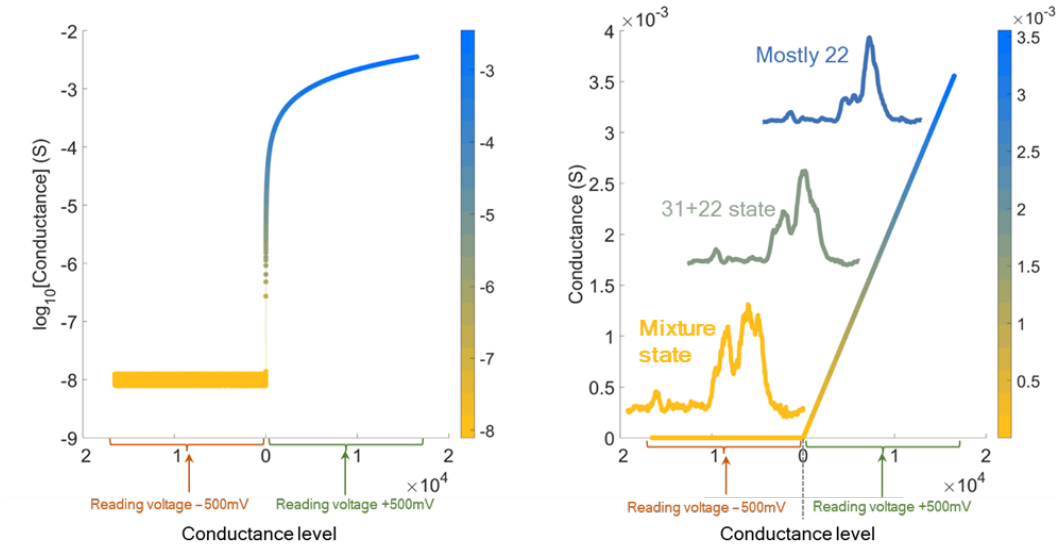


**Figure S10: Unidirectional read-out:** The in-situ Raman spectra measured during the read-out processes confirm that during negative read out, we indeed observe mixture of states comprising molecules in 3, 1 and 2 states characterised by $E_0$, $E_1$ and $E_2$ Raman modes. This is consistent with main text Fig. 3.

**Crosspoint integrity after a billion cycles:**

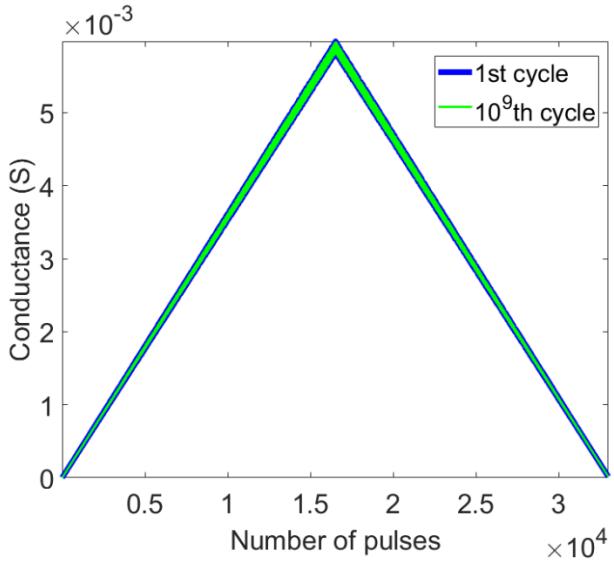


**Figure S11: Consistency after endurance test:** the weight update characteristics in the first and $10^{9th}$ cycles overlaid on top of each other showing no degradation.

**One pulse writing:**

For single pulse writing (Fig. 2), the initial state is 31. From there, potentiation pulses of different height and width were applied to write to different analog levels. In Fig. 2d we plot different $\Delta G_n = (G_n - G_1)$ values as a function of pulse width ($t_v$) and amplitude ($V_m$). We used 28 different $V_m$ and 589 $t_v$ values for each amplitude to achieve different $\Delta G_\eta$ values, as shown in the colour plot in Fig. S12. For any voltage below 830 mV there is no change in conductance. This sharp cut-off facilitates an efficient self-selection.

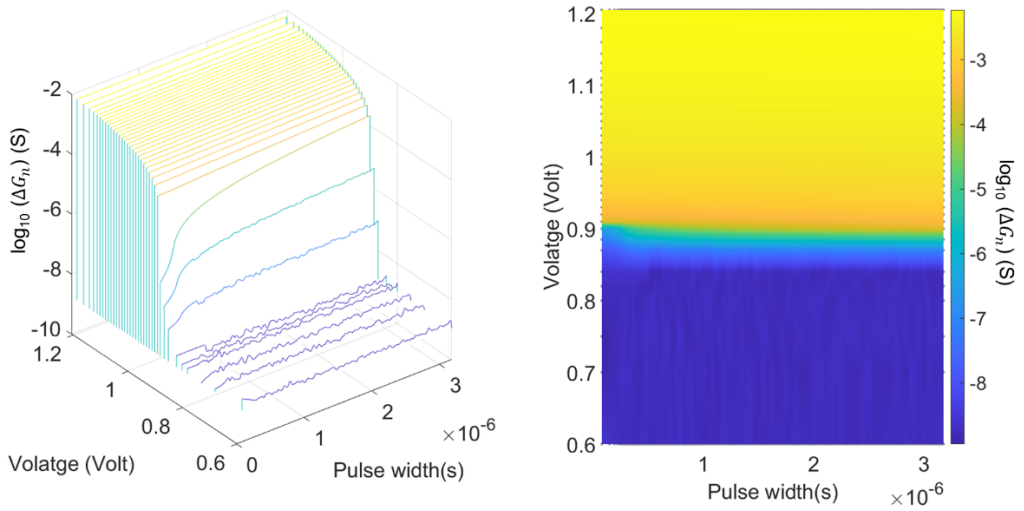


**Figure S12: One step writing:** Different values of $\Delta G_n$ expressed in terms of the colour intensity as a function of potentiation pulse width and amplitude.

## Section S4: In-situ Raman and molecular switching mechanism

### In-situ Raman:

Raman spectra of different analog states were measured after writing. To ensure the reliability of the measurements, we ensured the following:

1. We used a 785 nm laser. From the UV-VIS-NIR spectroscopy of our molecular compound, we concluded that the absorbance is close to zero at 785nm. Thus, optically induced heating should not alter the analog state.
2. We used a 0.01% neutral density (ND) filter, for which the laser power on the sample was 8 $\mu W/\mu m^2$.
3. With the ITO / $[Ru^{II}L_2]$ $(BF_4)_2$ (L = 2,6-bis(phenylazo)pyridine) / Au structure, we measured the analog weight update characteristic and found it to be linear and symmetric, as shown in Fig. S13, as observed with Au top and bottom electrodes (Fig. 1b).

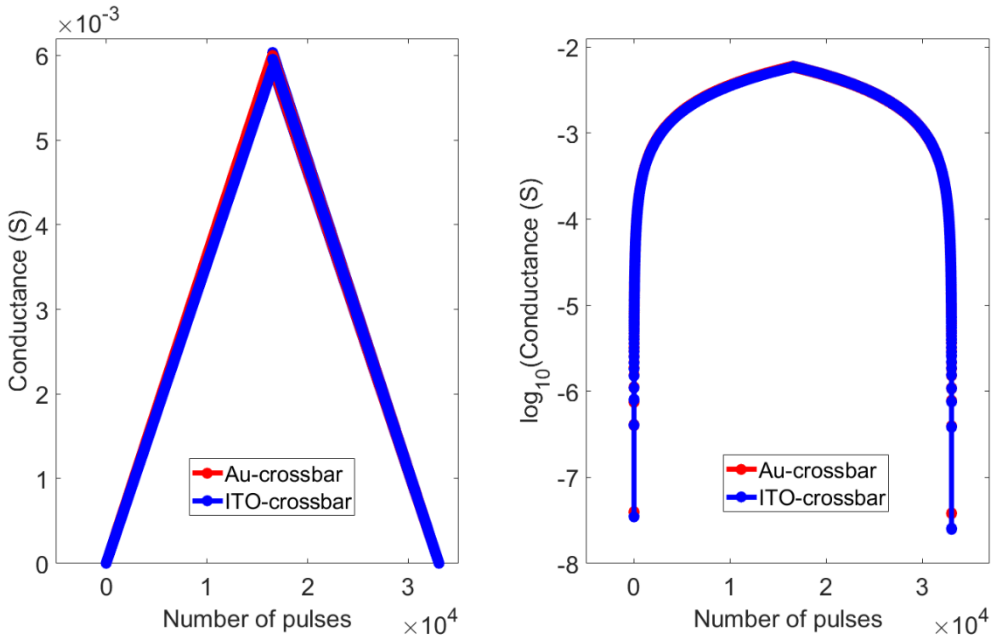


**Figure S13: characterization of ITO / $[Ru^{II}L_2]$ $(BF_4)_2$ / Au:** The weight update characteristics remained linear and symmetric on using transparent ITO as the top electrode.

The spectral traces were correlated to the molecular states as follows:

1. In the 22-state, as shown in Fig. S14, all ligands are singly reduced and because of two ligand per molecule, each molecule is two-electron reduced. Thus, in 22 a standalone $E_1$ mode is observed.
2. In the 31 state, on the first molecule, one ligand is two-electron reduced and the other in one-electron reduced, and on the second molecule, one ligand is one-electron reduced and the other is unreduced. This molecular electronic configuration has been confirmed in ref.[2,8], is pictorially shown in Fig. S14, and results in three azo vibrational modes $E_0$, $E_1$ and $E_2$ with relative intensities of 25%, 50% and 25%, respectively.
3. Consistent with the previous literature[2], during the transition from the 31 to the 22 states, the total intensity of the ($E_0$ + $E_1$ + $E_2$) modes remains nearly constant but their relative intensities change (Fig. S15a).
4. Based on the relative intensities of these modes, the fraction of the 31 and 22 states can be calculated using methods elaborated in ref.[2].
5. In this paper, we deliberately avoid the common acronym of DFT to describe these density functional theory electronic structure calculations, reserving it in this study for Discrete Fourier Transform, hence we refer below to these calculations as simply QM to denote the quantum mechanical methods used to compute the nuclear and electronic configurations inside the film. All crystal models and QM methods used were described in detail in ref.[2]. Here, we trace the path of counterions as the crystal unit cell is slightly expanded to allow some structural disorder in the film[2] and model the low-energy shuttling of the counterions between alternative binding pockets (main text Fig.3f). We calculated the energy change associated with displacement of the counterions from their starting binding pockets, with the electronic structure set at the starting high-spin 31 state.
6. We considered multiple counterion binding pockets in the film supramolecular structure, as visualised for a tetrameric $RuL_2(BF_4)_2$ assembly. Fig. S15b shows the corresponding volumetric expansion of the film up to 2% in the sub-150 meV energy window that triggers counterion displacements for low-energy migration between pockets, showing remarkable consistency with the experimentally measured activation barrier ~134 meV (Fig. 3c).

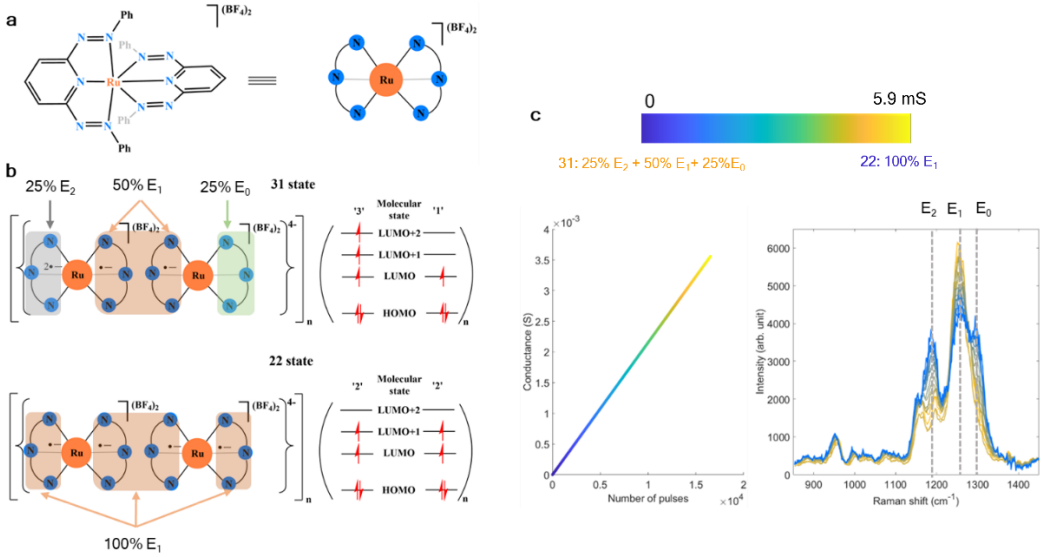


**Figure S14: Distribution of the 31 and 22 states:** (a) Schematic representation of $[Ru^{II}L_2](BF_4)_2$ (L = 2,6-bis(phenylazo)pyridine). (b) The ligand redox states of the molecule in the 31 and 22 states, and the expected population of the Raman modes. (c) The Raman spectral evolution during the potentiation process showing the transformation of the molecular film from all 31 state to all 22 state.

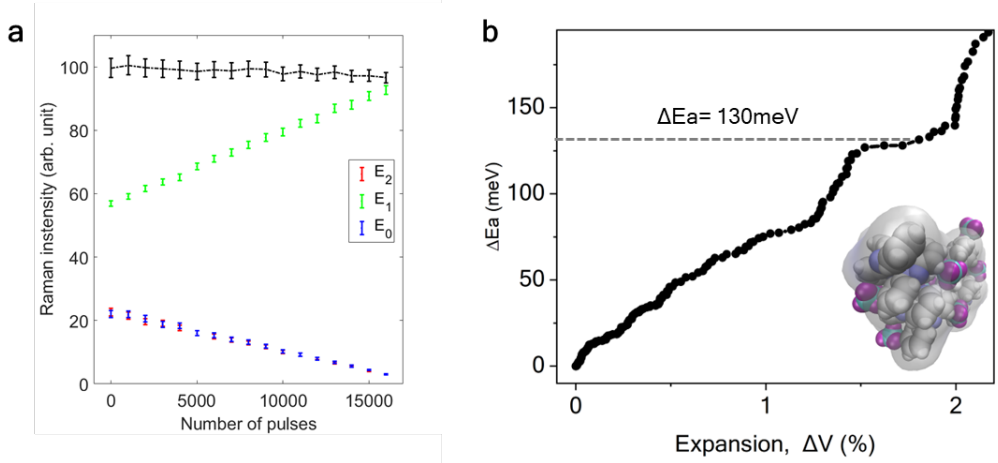


**Figure S15: Electronic states and counterion relaxation:** (a) The intensity of $E_0$, $E_1$ and $E_2$ as function of number of pulses ($n$). Notably the summed intensity ($E_0$+$E_1$+$E_2$, coloured black) is a near-constant, consistent with prior reports[2,8]. (b) The volumetric expansion resulted from the counterion relaxation at ~130mV corroborating the activation barrier observed in Fig. 3c. Inset: a perspective view, obtained by cutting a tetrameric 4-molecule unit together with its 4×2=8 counterions from the crystal unit cell and then encasing in a large vacuum cell to allow the counterions to relax and sample diverse binding pockets on the surface of the tetramer. The $BF_4$ counterion B atoms are cyan and F atoms are purple, and the tetramer is overlaid with a semi-transparent molecular surface.

**Modelling of the devices:**

The time required for transitioning the entire film from a 31 to a 22 state under an applied bias is kinetically limited, with timescale in microseconds[2]. When applying pulses of less than 100 nanoseconds, only a subpopulation of the total number of molecules transforms, resulting in the analog nature of the switching process.

To model this kinetic barrier-limited process, a nucleation-limited switching (NLS) approach, as described in equation S5, was employed. This method takes into account physical inhomogeneities in the local field, as elaborated and experimentally verified in previous studies[9,10]. From the initial 31 state, the fraction of molecules converted to 22 states after a specific number of pulses ($n$) can be expressed as:

$$f_{22}(n) = \frac{M_{22}(n)}{M_{22}(n)+M_{31}(n)} = \frac{1}{L}\sum_{z=1}^{z=L} Nr(z) = \frac{1}{L}\sum_{z=1}^{z=L}\left[\frac{1}{\pi} \times \arctan\left(\frac{n-\chi_N(\Phi_{mol}(z,n))}{\kappa_N(R)}\right) + \frac{1}{2}\right] \quad \text{(S5)}$$

$f_{22}(n)$ is the fraction of total number of molecules transformed to 22-state. $L$ is a parameter, proportional to the film thickness. $Nr$ denotes the rate of individual nucleation processes. The parameter $\kappa$ represents the rate of nucleation and $\chi$ refers to the centre of the nucleation processes. The transition of the entire film comprises multiple nucleation processes, each operating at an identical rate ($\kappa_N(R)$. The rate $R$ is constant, as inferred from Fig. 3c. The probability of seeding of these nucleation centres (i.e., $\chi_N$) is controlled by the electrostatic potential $\Phi_{mol}\ (z,\ n)$ along the thickness of the film. For different number of pulses, $\Phi_{mol}\ (z,\ n)$ is calculated using equation S6 (where $z$ is a variable representing different molecular positions along the film thickness) and is shown in Fig. S16a. Similar formulations have previously been used to map electrostatic profiles across molecular junctions[11-15].

$$\Phi_{mol}(z,n) = \Phi_0(z) - \frac{V_{max}}{\pi}\sum_{m=1}^{\infty}\frac{F_m}{m(1+F_m)}\left[C_1\, sin\left(\frac{m\pi}{L}z\right) - C_2\, sin\left(\frac{m\pi}{L}z'\right)\right] \quad \text{(S6)}$$

Here $\Phi_0(z)$ represents a linear potential profile which can be obtained by solving the Laplace equation in the absence of any charge build-up inside the film, given as,

$$\Phi_0(z) = -\frac{z}{L} \times V_{max}$$

$V_{max}$ is the pulse height $+900\ mV$. Additionally, in equation S6,

$$z' = L - z$$

$$F_m = \frac{1}{2}\left(\frac{\sigma}{\zeta(n)}\right)^2 e^{\chi}\int_{\chi}^{\infty} du\,\frac{e^{-u}}{u} \quad \text{(S6a)}$$

where $\chi = \frac{1}{2}(2\pi m\sigma)^2$ (S6b)

and $C_1 = \left[1 + 2 \times \left(\eta - \frac{1}{2}\right)\right], C_2 = \left[1 - 2 \times \left(\eta - \frac{1}{2}\right)\right]$

$\eta$ is the voltage division factor[16]. In equation S6a, the parameter $\sigma$ depends on the molecular dimensions. The screening length $\zeta$ is a function of the number of pulses, $n$ and can be expressed as:

$$\zeta(n) = [(\alpha_1 n) + \alpha_2] + [\beta_1 \times \exp(\beta_2 \times n)] \quad \text{(S6c)}$$

where, $\alpha$ and $\beta$ are numerical constants. In Fig. S16a we plotted $\Phi_{mol}(z,n)$ vs $z$ for different $n$ values.

Based on equation S5, the rate of transformation along the film thickness can be computed as[11,12,17]:

$$k_{ET}(z) = \frac{\gamma}{\sqrt{4\pi\lambda k_B T}} \times \int \exp\left[-\frac{\left(E_\lambda + \Delta G^0 - e\Phi_{mol}(z,\ n) + E\right)^2}{4\lambda k_B T}\right] \cdot \psi(E) \cdot dE \qquad \text{(S7)}$$

$$\text{where } \gamma = \left(\frac{2\pi}{\hbar} \times H_{31}^2\right) \qquad \text{(S7a)}$$

The transfer integral $H_{31}$ describes the energetic coupling between the molecule in the state 3 (Donor) and 1 (Acceptor), $E_\lambda$ corresponds to the reorganization energy required to change the counter-ion position from 31 to 22 state. Formally, $E_\lambda$ includes also a small contribution from internal reorganisation of the nuclei in the molecules themselves as the electronic state is changed. $\Delta G^0$ is the Gibbs free energy for the reaction. $\Phi_{mol}(z,n)$ represents the electrostatic potential at a particular $z$ location and $\psi(E)$ is the acceptor density of states at energy $E$. $k_B$ is the Boltzmann constant and $T$ is the operating temperature.

The $dt = \gamma^{-1}$ determines the time scale for electron transfer and the probability of an electron transfer can be given as

$$\theta(z) = k_{ET}(z) \times dt \qquad \text{(S7b)}$$

Whether a particular z-site is activated can be expressed by the Heaviside function[12] $\varepsilon$ being a stochastic thresholding parameter as discussed in ref.[12],

$$P(z) = \int_{-\infty}^{\theta(z)-\varepsilon} \delta(x)\, dx \qquad \text{(S7c)}$$

Based on the equation S5-S7 we computed the $f_{22}(n)$ and $f_{31}(n) = 1 - f_{22}(n)$, as shown in Fig. S16c.

Fig. S16b shows the propagation of multiple nucleation processes along the film thickness, i.e., $Nr(z)$ in equation S5. The overlaps between the linear regimes of the individual nucleation processes ($Nr(z)$) account for the observed linearity in Raman and electrical measurements. The calculated fraction of molecules in the 22-state as a function of the number of pulses is shown in Fig. S16.

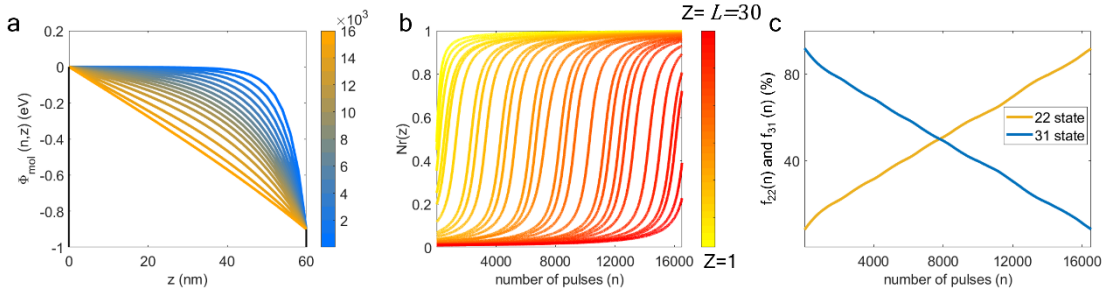


**Figure S16: Calculated rate of molecular transformation:** (a) Calculated $\Phi_{mol}(z)$ for different $n$ values. **Note:** In Fig. 3h, we plotted $\Phi_{mol}(z)$ versus $z$ during the reading process formulated with different screening lengths as described in the main text. (b) The computed

individual nucleation rates $Nr(z)$ captured in eqn. S5, *i.e.*, $Nr(z) = [\frac{1}{\pi} \times \arctan\left(\frac{n-\chi_N(\Phi_{mol}(z,n))}{\kappa_N(R)}\right) + \frac{1}{2}]\ \forall\ z \in [1, \lambda]$, versus $n$. Curves are plotted for different $z$ values (i.e., position along the film). (c) Calculated $\%f_{22}(n)$ and $\%f_{31}(n)$ with increasing number of pulses.

**Comment on the time scale of measurement: analog vs digital switching:** The time required to convert all the molecules in a film from 31 to 22 or vice versa is on the order of several microseconds[1,2]. Here because of the sub-100ns pulses, the process is kinetically limited and we observe a gradual transition. On applying a voltage with much larger pulse width, we can completely transform the film from 31 to 22 resulting in a digital transition. Application of further higher positive voltages would transform it to the 11-state, as reported in previous papers on the same molecular systems[1,2].

## Section S5: Measurement of VMM in the crossbar

**Wire resistance correction for simultaneously reading the entire crossbar (all rows and columns selected):**

For simultaneous reading, there are many parallel current paths and hence each node voltage ($V_{p,q}$ ) needs to be computed as a function of $V_p$, $V_{Gq}$, $R_{p,q}$, $\rho$ and $\chi$.

$$V_{p,q} = \gamma . \begin{bmatrix} V_{p,q+1} \\ V_{p,q-1} \\ V_{Gq} \end{bmatrix} \forall\, p \in [1,N]\ and\ q \in [1,N] \quad \text{(S8)}$$

Where,

$$\gamma = \left[ \begin{pmatrix} \left(\frac{R_{p,q,\chi}}{2R_{p,q,\chi}+\rho} & \frac{R_{p,q,\chi}}{2R_{p,q,\chi}+\rho} & \frac{\rho}{2R_{p,q,\chi}+\rho}\right) \forall\, p \in [1,N]\ and\ q \in [1,N) \\ \left(0 \quad \frac{R_{p,q,\chi}}{R_{p,q,\chi}+\rho} \quad \frac{\rho}{R_{p,q,\chi}}\right) \forall\, p = [1,N]\ and\ q = N \end{pmatrix} \right]$$

By solving these equations, all $V_{p,q}$ values can be obtained.

$\Delta V_{p,q,\rho} = (V_{p0} - V_{p,q})$ gives the difference between the DAC voltage and a node voltage representing the drop along the $p^{th}$ row.

Similarly, $\Delta V_{p,q,\chi} = (V_{p,q} - V_{G,q})$ is the wire resistance drop along the $q^{th}$ column.

$$I_q = \sum_{p=1}^{N} \frac{V_{p,q} - V_{Gq}}{R_{p,q} + (S-p+1)\chi} \qquad \forall\, p \in [1,N]\ and\ q \in [1,N]\ , \quad \text{(S9)}$$

where, $R_{p,q,\chi} = R_{p,q} + (N-p+1)\chi$

$$I_{q\_ideal} = \sum_{p=1}^{N} \frac{V_{p0}}{R_{p,q}} \qquad \forall\, p \in [1,N]\ and\ \ q \in [1,N] \quad \text{(S10)}$$

$$\left(I_{q\_ideal} - I_q\right) = \sum_{p=1}^{N} \frac{V_0}{R_{p,q}} - \frac{V_{p,q} - V_{G,q}}{R_{p,q} + (N-p+1)\chi} \qquad \forall\, p \in [1,N]\ and\ q \in [1,N] \quad \text{(S11)}$$

$$\left(I_{q\_ideal} - I_q\right) = \Delta I_q = \sum_{p=1}^{N} \frac{\Delta V_{p,q} - V_{G,q}}{R_{p,q,\chi}} + \frac{V_{p,0}}{R_{p,q}} \qquad \forall\, p \in [1,N]\ and\ q \in [1,N] \quad \text{(S12)}$$

These calculations are consistent with previous publications[6,7,18,19] and as it has been shown, for wire resistance values <1Ω per block, the overhead for calculating wire resistance

compensation is not substantial. We numerically solved the node equations. A few iterations (depending on the type of matrix) were sufficient to obtain the presented error values. We employed a sparse matrix based KCL and KVL solver in Matlab that has been previously implemented and known to be orders of magnitude faster and simpler than conventional or analytical techniques[20-22]. In addition, there are swift regression methods to solve similar problems as highlighted in ref.[23-26].

We used an extra row to source this additional amount of current[27].

The node voltages of the extra row can be given as

$$V_{N+1,q} = V_{N+1,0} - N.\rho \quad \text{(S13)}$$

and the cross-point resistances can be calculated as

$$R_{N+1,q} = \frac{V_{N+1,q}}{\Delta I_q} \; \forall \; p = N+1 \; and \; q \in [1, N] \quad \text{(S14)}$$

Thus, the compensation is achieved within the crossbar and the accuracy of our VMM results further support our claims of accurate wire resistance compensation.

**Additional corrections:**

There can be other sources of errors such DAC offset and those induced by the op-amps in the circuits. The simple linear equation required for DAC calibration (similar to that reported in ref.[22]) was handwritten in the firmware. Similarly, for the op-amp offset correction, we fed the non-inverting terminal (the virtual ground potential) from a DAC where the offset can be compensated[28]. These were one-time operations and so, hardly cause additional overhead.

With these corrections implemented in our circuit, we measured the correlation between the VMM output our crossbar output and the software calculated data. The software calculations were done using target conductance values at each cross point along with experimentally determined row and column wire resistances (0.46 Ω per block in the rows and 0.39 Ω per block in columns). The standard deviation between the calculated VMM output and the measure value was 206 nA which is remarkable and provide opportunities for development of algorithms for obtaining nearly ideal results using this platform.

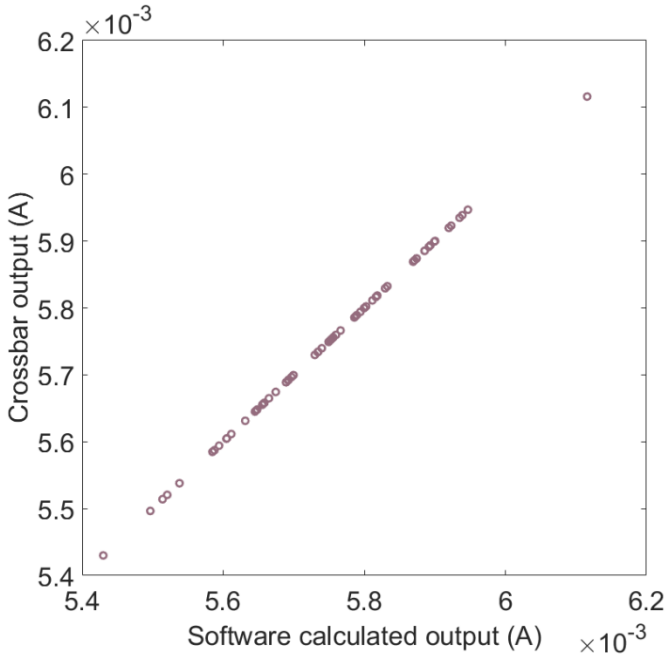


**Figure S17: Experimental accuracy:** The measured crossbar VMM output vs the simulated VMM result.

## Section S6: Demonstration of vector matric multiplication (VMM)

**Discrete Fourier Transform (DFT):**

Discrete Fourier transform can be expressed as:

$$X = x.W \tag{S15}$$

Where,

$x = [x_1, x_2, x_3 \cdots, x_N]_{1\times N}$ is input real number i.e., $x \in \mathbb{R}^{1\times N}$

$X = [X_1, X_2, X_3 \cdots, X_N]_{1\times N}$ is output complex number i.e., $X \in C^{1\times N}$

$W_{N\times N}$ is the DFT matrix ($W \in C^{N\times N}$) expressed as

$$W = \frac{1}{\sqrt{N}} \cdot \begin{bmatrix} 1 & 1 & 1 & 1 & \dots & 1 \\ 1 & \omega & \omega^2 & \omega^3 & \dots & \omega^{(N-1)} \\ 1 & \omega^2 & \omega^4 & \omega^6 & \dots & \omega^{2(N-1)} \\ 1 & \omega^3 & \omega^6 & \omega^9 & \dots & \omega^{3(N-1)} \\ . & . & . & . & . & . \\ . & . & . & . & . & . \\ . & . & . & . & . & . \\ 1 & \omega^{N-1} & \omega^{2(N-1)} & \omega^{3(N-1)} & \dots & \omega^{(N-1).(N-1)} \end{bmatrix}$$

Where $\omega = e^{-j\cdot\left(\frac{2\pi}{N}\right)}$

$X$ and $W$ can be expressed as:

$X = Re(X) + j \cdot Im(X)$

and

$W_{p,q} = Re\left(W_{p,q}\right) + j \cdot Im\left(W_{p,q}\right)$

$p, q \in \mathbb{R}^{1\times N}$

The DFT matrix can be mapped to the conductance values using eqn. S16, S17.

$$\left[G_{p,q}\right]_{\substack{p=1:\left(\frac{N}{2}+1\right) \\ q=1:\left(\frac{N}{2}+1\right)}} = \left[1 \quad Re\left(W_{p,q}\right)\right] \cdot \begin{bmatrix} \frac{G_{max}+G_{min}}{2} \\ \frac{G_{max}-G_{min}}{2} \end{bmatrix} \tag{S16}$$

$$\left[G_{p,q}\right]_{\substack{p=\left(\frac{N}{2}+2\right):N \\ q=\left(\frac{N}{2}+2\right):N}} = \left[1 \quad Im\left(W_{p,q}\right)\right] \cdot \begin{bmatrix} \frac{G_{max}+G_{min}}{2} \\ \frac{G_{max}-G_{min}}{2} \end{bmatrix} \tag{S17}$$

The DFT output can be written as:

$$[X_q]_{1\times N} = \sum_{p=1}^{N} [x_p]_{1\times N} . [W_{p,q}]_{N\times N} \; \forall \; q \; \in [1, \; N]$$

$$= \sum_{p=1}^{N} [x_p]_{1\times N} . \left[Re(W_{p,q}) + j \cdot Im(W_{p,q})\right]_{N\times N}$$

$$= \sum_{p=1}^{N} [x_p]_{1\times N} . Re(W_{p,q})_{N\times N} \; + \; j . \sum_{p=1}^{N} [x_p]_{1\times N} . Im(W_{p,q})_{N\times N} \qquad \text{(S18)}$$

The symmetry of $Re(W_{p,q})$ and $Im(W_{p,q})$, (between $q \; \in \left[1, \frac{N}{2}\right] and \; q \in (\frac{N}{2} + 1, N]$) would be inherited in the output, *i.e.*, in $Re(X_q)$ and $Im(X_q)$. Hence, rather than utilizing the entire range (*i.e.*, $q = 1 \; to \; N$) we can utilize only half of the range *i.e.*, $q \; \in \left[1, \frac{N}{2}\right]$ and write the equation S18 as follows:

$$Re[X_q]_{1\times\frac{N}{2}} = \sum_{p=1}^{N} [x_p]_{1\times N} . Re(W_{p,q})_{N\times\frac{N}{2}} \quad \forall \; q \; \in \left[1, \frac{N}{2}\right] \qquad \text{(S19)}$$

This operation will be utilised in half of the total number of the columns. Similarly, the imaginary part can be computed as:

$$Im[X_q]_{1\times\frac{N}{2}} = \sum_{p=1}^{N} [x_p]_{1\times N} . Im(W_{p,q})_{N\times\frac{N}{2}} \quad \forall \; q \; \in \left[1, \frac{N}{2}\right] \qquad \text{(S20)}$$

Since in a dot product engine this multiply and accumulation occurs in the crossbar, the output is current, input will be voltage and the conductance values will be programmed in the matrix. We define variables $P$ and $Q$ to represent the row and column of the crossbar that can be related to the DFT matrix dimensions, $p$ and $q$ as follows,

$P = \; p$ and for $Q \; \in \left[1, \frac{N}{2}\right], q = Q$ , for $\forall \; Q \; \in \left(\frac{N}{2}, N\right], q = J - \frac{N}{2}$

Hence, the eqn. S19 and S20 can be written as:

$$Re[I_Q]_{1\times\frac{N}{2}} = \sum_{I=1}^{N} [v_p]_{1\times\frac{N}{2}} . Re(G_{p,q})_{N\times\frac{N}{2}} \quad \forall \; Q \; \in \left[1, \frac{N}{2}\right] \; (q = Q) \qquad \text{(S21)}$$

$$Im[I_Q]_{1\times\frac{N}{2}} = \sum_{I=1}^{N} [v_p]_{1\times\frac{N}{2}} . Im(G_{p,q})_{N\times\frac{N}{2}} \; \forall Q \; \in \left(\frac{N}{2}, N\right] \; (\; q = Q - \frac{N}{2}) \qquad \text{(S22)}$$

So, $G_{P,Q} = Re(G_{p,q}) \quad \forall \; I \in [1, N] and \; Q \; \in \left[1, \frac{N}{2}\right] (q = Q)$

$G_{P,Q} = Im(G_{p,q}) \; \forall \; P \in [1, N] and \; Q \; \in \left(\frac{N}{2}, N\right] \; (\; q = Q - \frac{N}{2})$

Here $P_q$ is a specific column current. Combinations of all such column current contains all frequency information which can be further re-normalised by incorporating the symmetric and antisymmetric properties of DFT matrix for specific application.

**Inverse Discrete Fourier Transform (IDFT):**

IDFT, following the same conventions as in DFT, can be expressed as

$$x = \frac{1}{N}(X.\ W^*)$$

$$W = \frac{1}{\sqrt{N}} \cdot \begin{bmatrix} 1 & 1 & 1 & 1 & \dots & 1 \\ 1 & \omega & \omega^2 & \omega^3 & \dots & \omega^{(N-1)} \\ 1 & \omega^2 & \omega^4 & \omega^6 & \dots & \omega^{2(N-1)} \\ 1 & \omega^3 & \omega^6 & \omega^9 & \dots & \omega^{3(N-1)} \\ . & . & . & . & . & . \\ . & . & . & . & . & . \\ . & . & . & . & . & . \\ 1 & \omega^{N-1} & \omega^{2(N-1)} & \omega^{3(N-1)} & \dots & \omega^{(N-1).(N-1)} \end{bmatrix}$$

where $\omega = e^{-j\cdot\left(\frac{2\pi}{N}\right)}$

$$x = \frac{1}{N}(X_{1\times N}.\ {W^*}_{N\times N}) = \frac{1}{N}\left(Re(X_{1\times N}) + j\ Im(X_{1\times N})\right).\left(Re(W_{N\times N}) - j\ Im(W_{N\times N})\right)$$

$$= \frac{1}{N}\left([Re(X)]_{1\times N}.[Re(W)]_{N\times N} + [Im(R)]_{1\times N}.[Im(W)]_{N\times N}\right) + j([Im(X)]_{1\times N}.[Re(W)]_{N\times N} - [Re(X)]_{1\times N}.[Im(W)]_{N\times N}) \quad \text{(S23)}$$

Each of these terms can be calculated using the dot product engine using the same method described above for DFT where, $W_{p,q}$ ($\forall\ p \in [1,N] and\ q \in [1,N]$) can be mapped to $G_{P,Q}$ ($\forall\ P \in [1,N] and\ Q \in [1,N]$) where $P$ and $Q$ are the index of the row and column in a crossbar. The input still remains the voltage and the output of the vector matrix multiplication is the current.

**DFT Matrix writing accuracy:**

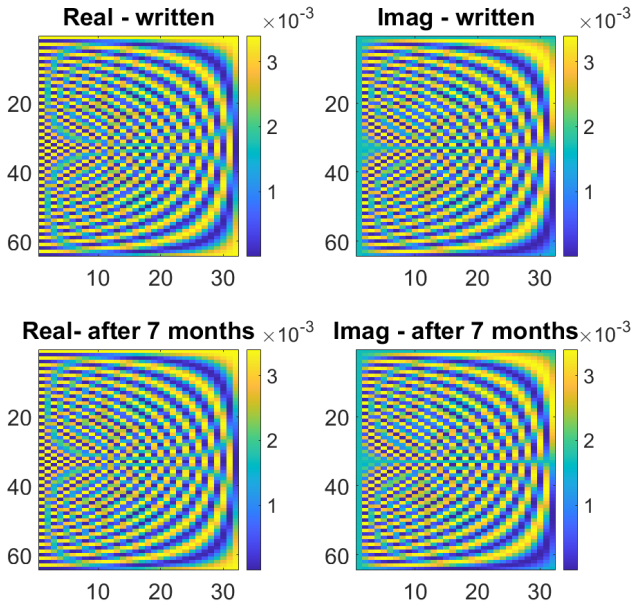


**Figure S18: Retention of DFT matrix:** After writing the cross points, they were immidiately read. Subsequently the crossbar was kept for 7 months without any voltage and was re-read. All the written values were retained.

**DFT of different representative waveforms:**

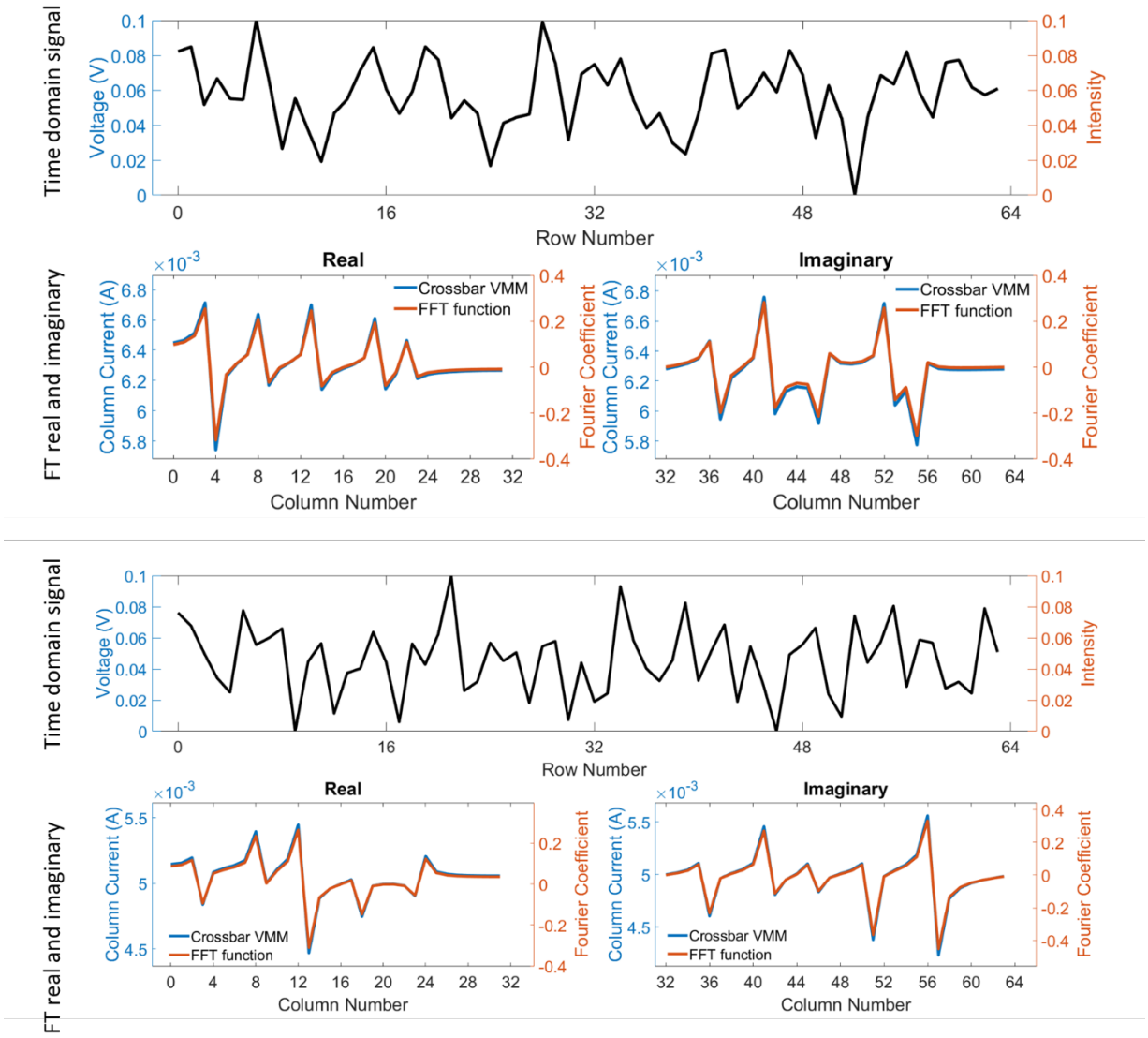


**Figure S19: Robustness of our FT calculation:** The FT calculated by our dot product engine (in one-step) from different time domain signals yielded an excellent match with the software calculated results.

**Reconstruction of original waveform via IDFT:**

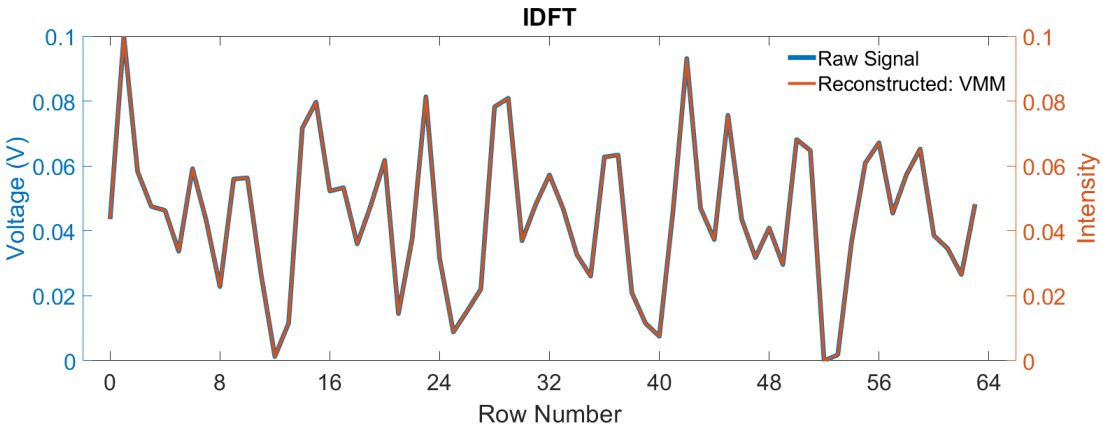


**Figure S20: IDFT signal integrity:** The FT results calculated by out dot product engine (DPE) was further used for calculating the DPE based IDFT yielding an excellent match with the original signal.

**Image reconstruction:**

For image reconstruction, we used the high-resolution James Web Telescope data available from the NASA repository[29]. In Matlab we separated the color dimensions (red, blue, and green) and generated one-dimensional vectors. A 64-point discrete Fourier transform (DFT) was applied to each of the three-color planes. The real and imaginary components of the frequency domain were multiplied with our conductance matrix (IDFT). The input was time-multiplexed with each comprising 64 input pixels, which were normalized to 100 mV range. The output of each step was merged to reconstruct the image. This is a common procedure followed in previous publications[22,30].

For the space image reconstruction illustrated in Fig. 4, a total of 5,041,230 inputs were utilized for the R, G, and B planes, equating to 1,680,410 inputs per plane. The input array's size sent to the crossbar was 64×1. Therefore, the steps needed for the reconstruction of each plane were calculated as 1,680,410/64 = 26,256 steps. In contrast, a comparable 64-point DFT executed on a digital computer would necessitate 107,545,941 steps. In this hardware reconstruction, a Peak Signal-to-Noise Ratio (PSNR) of 76.5 dB and a Signal-to-Noise Ratio (SNR) of 74 dB were achieved. SNR and PSNR for a matrix-matrix multiplication was calculated by comparing the target and the experimentally determined matrices using equation S24 and S25, respectively.

$$SNR = 20 \cdot log_{10}\left(\frac{\sum_{p=0}^{m-1}\sum_{q=0}^{n-1} x_{p,q}}{\sum_{p=0}^{m-1}\sum_{q=0}^{n-1}(x_{p,q}-L_{p,q})}\right) \quad \text{(S24)}$$

where, $x_{p,q}$ represents a noise-free reference matrix, and $L_{p,q}$ represents the reconstructed experimental data. Here $p$ and $p$ refer to specific rows and columns respectively, which can vary within the range of 'm' and 'n' respectively.

$$PSNR = 20 \cdot log_{10}\left(\frac{MAX}{\sqrt{MSE}}\right) \quad \text{(S25)}$$

Where $MAX$ refers to the maximum possible value in the reference matrix which is obtained from spatial information of original image and mean square error MSE can be expressed as:

$$MSE = \frac{1}{p \cdot q} \cdot \sum_{p=0}^{m-1} \sum_{q=0}^{n-1} \left[x_{p,q} - L_{p,q}\right]^2 \quad \text{(S26)}$$

**Estimation of Power efficiency:**

The system's overall power efficiency was determined, considering the peripheral circuitry. This assessment serves as an approximate measure of the expected performance from a system on a chip (SoC) employing this accelerator. In its current setup on a printed circuit board, deliberately unoptimized components were used with reduced speed, emphasizing maximum precision. Below, we present two designs aiming for an energy-optimized system that still meets precision requirements.

To ensure a low-noise output signal, the op-amp OPA838 (ref. [31]) was considered for the Transimpedance Amplifier (TIA). With a power consumption of 4.8mW and an input-referred noise of 1.8nV/√Hz at a 300MHz Gain-Bandwidth, it provides a system bandwidth of 50MHz considering the closed-loop gain of the op-amp in combination with the parallel memristor in the crossbar and the TIA feedback resistor. Paired with a 13-bit, 50 MSPS ADC design[32] consuming 4.2mW per channel, their integration yields an estimated energy efficiency of (64×64×2) ×50MHz / (64 × (4.8mW + 4.2mW)) = 0.7 TOPS/W.

Alternatively, considering a compromise to a single-bit precision, the use of a 12-bit ADC mentioned in ref. [33], operating at a 20 MSPS rate with a power consumption of 0.47mW per channel, along with an op-amp detailed in ref. [34], delivers an energy efficiency calculation of (64×64×2) ×20MHz / (64 × (0.16mW+ 0.47mW)) = 4.1 TOPS/W. This significantly surpasses the 18-core Haswell CPU[35] (8.96 GOPS/W using 8-bit precision) by 460 times while offering a 4-bit precision upgrade. This estimated power efficiency is also 220× larger than a NVIDIA K80 GPU (18.66 GOPS/W) [35]. Notably, the crossbar's power consumption is 0.1V ×20mA = 2mW, considerably lower than the contribution from peripheral elements.

A trade-off between the output precision and energy consumption could be considered based on the priority of the intended applications. Moreover, these energy efficiency values were compiled from different studies. Also, for a larger crossbar, this energy efficiency would be further improved, because of the scaling as a function of array size. In short, anticipated future integration and system optimization on a single chip using advanced technology nodes are expected to yield significant energy savings beyond 4.1 TOPS/W.

## References:


1 Rath, S. P., Thompson, D., Goswami, S. & Goswami, S. Many-Body Molecular Interactions in a Memristor. *Advanced Materials*, 2204551 (2022).

2 Goswami, S. *et al.* Charge disproportionate molecular redox for discrete memristive and memcapacitive switching. *Nature nanotechnology* **15**, 380-389 (2020).

3 Shi, L., Zheng, G., Tian, B., Dkhil, B. & Duan, C. Research progress on solutions to the sneak path issue in memristor crossbar arrays. *Nanoscale Advances* **2**, 1811-1827 (2020).

4 Vontobel, P. O. *et al.* Writing to and reading from a nano-scale crossbar memory based on memristors. *Nanotechnology* **20**, 425204 (2009).

5 Li, H. *et al.* Memristive crossbar arrays for storage and computing applications. *Advanced Intelligent Systems* **3**, 2100017 (2021).

6 Liao, Y. *et al.* Diagonal matrix regression layer: Training neural networks on resistive crossbars with interconnect resistance effect. *IEEE Transactions on Computer-Aided Design of Integrated Circuits and Systems* **40**, 1662-1671 (2020).

7 Jeong, Y., Zidan, M. A. & Lu, W. D. Parasitic effect analysis in memristor-array-based neuromorphic systems. *IEEE Transactions on Nanotechnology* **17**, 184-193 (2017).

8 Goswami, S. *et al.* Robust resistive memory devices using solution-processable metal-coordinated azo aromatics. *Nature materials* **16**, 1216-1224 (2017).

9 Boyn, S. *et al.* Learning through ferroelectric domain dynamics in solid-state synapses. *Nature communications* **8**, 14736 (2017).

10 Jo, J. *et al.* Domain switching kinetics in disordered ferroelectric thin films. *Physical review letters* **99**, 267602 (2007).

11 Migliore, A. & Nitzan, A. Nonlinear charge transport in redox molecular junctions: A Marcus perspective. *Acs Nano* **5**, 6669-6685 (2011).

12 Schwarz, F. *et al.* Field-induced conductance switching by charge-state alternation in organometallic single-molecule junctions. *Nature nanotechnology* **11**, 170-176 (2016).

13 Liang, G., Ghosh, A., Paulsson, M. & Datta, S. Electrostatic potential profiles of molecular conductors. *Physical Review B* **69**, 115302 (2004).

14 Yuan, L. *et al.* Controlling the direction of rectification in a molecular diode. *Nature communications* **6**, 6324 (2015).

15 Nitzan, A., Galperin, M., Ingold, G.-L. & Grabert, H. On the electrostatic potential profile in biased molecular wires. *The Journal of chemical physics* **117**, 10837-10841 (2002).

16 Moth-Poulsen, K. & Bjørnholm, T. Molecular electronics with single molecules in solid-state devices. *Nature nanotechnology* **4**, 551-556 (2009).

17 Kastlunger, G. & Stadler, R. Bias-induced conductance switching in single molecule junctions containing a redox-active transition metal complex. *Monatshefte für Chemie-Chemical Monthly* **147**, 1675-1686 (2016).

18 Zoppo, G. *et al.* in *2022 19th International SoC Design Conference (ISOCC).* 249-250 (IEEE).

19 Lepri, N. *et al.* Modeling and compensation of IR drop in crosspoint accelerators of neural networks. *IEEE Transactions on Electron Devices* **69**, 1575-1581 (2022).

20 Hu, M., Strachan, J. P., Zhiyong, L., Stanley, & Williams, R.S. International Symposium on Quality Electronic Design (ISQED), 374-379 (Santa Clara, CA, USA, 2016). (2016).

21 Hu, M. e. a. Proceedings of the 53rd Annual Design Automation Conference. 1-6 (Austin, Texas, 2016). .

22 Li, C. *et al.* Analogue signal and image processing with large memristor crossbars. *Nature electronics* **1**, 52-59 (2018).

23 Shi, J., Yin, W., Osher, S. & Sajda, P. A fast hybrid algorithm for large-scale l1-regularized logistic regression. *The Journal of Machine Learning Research* **11**, 713-741 (2010).

24 Rupp, M., Tkatchenko, A., Müller, K.-R. & Von Lilienfeld, O. A. Fast and accurate modeling of molecular atomization energies with machine learning. *Physical review letters* **108**, 058301 (2012).

25 McConaghy, T. FFX: Fast, scalable, deterministic symbolic regression technology. *Genetic Programming Theory and Practice IX*, 235-260 (2011).
26 Acharya, J., Diakonikolas, I., Li, J. & Schmidt, L. in *International Conference on Machine Learning.* 2878-2886 (PMLR).
27 Korkmaz, A. *et al.* Spectral Ranking in Complex Networks Using Memristor Crossbars. *IEEE Journal on Emerging and Selected Topics in Circuits and Systems* **13**, 357-370 (2023).
28 Korkmaz, A. *et al.* in *2023 IEEE International Symposium on Circuits and Systems (ISCAS).* 1-5 (IEEE).
29 *James Webb Space Telescope Repository, https://webbtelescope.org/images*.
30 Zhao, H. *et al.* Energy-efficient high-fidelity image reconstruction with memristor arrays for medical diagnosis. *Nature Communications* **14**, 2276 (2023).
31 Instruments, T. OPA838: 1-mA, 300-MHz Gain Bandwidth, Voltage-Feedback Op Amp. *Data sheet*.
32 Miki, T. *et al.* A 4.2 mw 50 ms/s 13 bit CMOS SAR ADC with SNR and SFDR enhancement techniques. *IEEE Journal of Solid-State Circuits* **50**, 1372-1381 (2015).
33 Shehzad, K. *et al.* A low-power 12-bit 20 MS/s asynchronously controlled SAR ADC for WAVE ITS sensor based applications. *Sensors* **21**, 2260 (2021).
34 Zoppo, G. *et al.* Analog solutions of discrete Markov chains via memristor crossbars. *IEEE Transactions on Circuits and Systems I: Regular Papers* **68**, 4910-4923 (2021).
35 Jouppi, N. P. *et al.* in *Proceedings of the 44th annual international symposium on computer architecture.* 1-12.